Thin-disk pumped optical parametric chirped pulse amplifier delivering CEP-stable multi-mJ few-cycle pulses at 6 kHz

Stephan Prinz,[1,2,*] Maximilian Schnitzenbaumer,[2] Dionysios Potamianos,[2,3] Marcel Schultze,[1] Sebastian Stark,[1] Matthias Häfner,[1] Catherine Y. Teisset,[1] Christoph Wandt,[1] Knut Michel,[1] Reinhard Kienberger,[2,3] Birgitta Bernhardt,[2,4] and Thomas Metzger[1]

[1]*TRUMPF Scientific Lasers GmbH + Co. KG, Feringastr. 10a, 85774 Unterföhring, Germany*
[2]*Department of Physics, Technische Universität München, James-Franck-Str., 85748 Garching, Germany*
[3]*Max-Planck-Institut für Quantenoptik, Hans-Kopfermann-Str. 1, 85748 Garching, Germany*
[4]*Abbe Center of Photonics, Friedrich Schiller University Jena, 07745 Jena, Germany*
*stephan.prinz@de.trumpf.com

Abstract: We present an optical parametric chirped pulse amplifier (OPCPA) delivering CEP-stable ultrashort pulses with 7 fs, high energies of more than 1.8 mJ and high average output power exceeding 10 W at a repetition rate of 6 kHz. The system is pumped by a picosecond regenerative thin-disk amplifier and exhibits an excellent long-term stability. In a proof-of-principle experiment, high harmonic generation is demonstrated in neon up to the 61st order.

References and links

1. F. Krausz and M. I. Stockman, "Attosecond metrology: from electron capture to future signal processing," Nat. Photonics **8**(3), 205–213 (2014).
2. M. Chini, K. Zhao, and Z. Chang, "The generation, characterization and applications of broadband isolated attosecond pulses," Nat. Photonics **8**(3), 178–186 (2014).
3. A. Sommer, E. M. Bothschafter, S. A. Sato, C. Jakubeit, T. Latka, O. Razskazovskaya, H. Fattahi, M. Jobst, W. Schweinberger, V. Shirvanyan, V. S. Yakovlev, R. Kienberger, K. Yabana, N. Karpowicz, M. Schultze, and F. Krausz, "Attosecond nonlinear polarization and light-matter energy transfer in solids," Nature **534**(7605), 86–90 (2016).
4. F. Böhle, M. Kretschmar, A. Jullien, M. Kovacs, M. Miranda, R. Romero, H. Crespo, U. Morgner, P. Simon, R. Lopez-Martens, and T. Nagy, "Compression of CEP-stable multi-mJ laser pulses down to 4 fs in long hollow fibers," Laser Phys. Lett. **11**(9), 095401 (2014).
5. T. Nagy, V. Pervak, and P. Simon, "Optimal pulse compression in long hollow fibers," Opt. Lett. **36**(22), 4422–4424 (2011).
6. S. Bohman, A. Suda, T. Kanai, S. Yamaguchi, and K. Midorikawa, "Generation of 5.0 fs, 5.0 mJ pulses at 1kHz using hollow-fiber pulse compression," Opt. Lett. **35**(11), 1887–1889 (2010).
7. G. Sansone, L. Poletto, and M. Nisoli, "High-energy attosecond light sources," Nat. Photonics **5**(11), 655–663 (2011).
8. E. J. Takahashi, P. Lan, O. D. Mücke, Y. Nabekawa, and K. Midorikawa, "Attosecond nonlinear optics using gigawatt-scale isolated attosecond pulses," Nat. Commun. **4**, 2691 (2013).
9. P. Rudawski, "Carrier-envelope phase dependent high-order harmonic generation with a high-repetition rate OPCPA-system," Eur. Phys. J. D **69**(70), 1434–6060 (2015).
10. A. Baltuška, T. Fuji, and T. Kobayashi, "Controlling the Carrier-Envelope Phase of Ultrashort Light Pulses with Optical Parametric Amplifiers," Phys. Rev. Lett. **88**(13), 133901 (2002).
11. J. Rothhardt, S. Demmler, S. Hädrich, J. Limpert, and A. Tünnermann, "Octave-spanning OPCPA system delivering CEP-stable few-cycle pulses and 22 W of average power at 1 MHz repetition rate," Opt. Express **20**(10), 10870–10878 (2012).

12. S. Prinz, M. Haefner, C. Y. Teisset, R. Bessing, K. Michel, Y. Lee, X. T. Geng, S. Kim, D. E. Kim, T. Metzger, and M. Schultze, "CEP-stable, sub-6 fs, 300-kHz OPCPA system with more than 15 W of average power," Opt. Express **23**(2), 1388–1394 (2015).

13. D. Herrmann, L. Veisz, R. Tautz, F. Tavella, K. Schmid, V. Pervak, and F. Krausz, "Generation of sub-three-cycle, 16 TW light pulses by using noncollinear optical parametric chirped-pulse amplification," Opt. Lett. **34**(16), 2459–2461 (2009).

14. R. Budriūnas, T. Stanislauskas, J. Adamonis, A. Aleknavičius, G. Veitas, D. Gadonas, S. Balickas, A. Michailovas, and A. Varanavičius, "53 W average power CEP-stabilized OPCPA system delivering 5.5 TW few cycle pulses at 1 kHz repetition rate," Opt. Express **25**(5), 5797–5806 (2017).

15. C. Teisset, N. Ishii, T. Fuji, T. Metzger, S. Köhler, R. Holzwarth, A. Baltuska, A. Zheltikov, and F. Krausz, "Soliton-based pump-seed synchronization for few-cycle OPCPA," Opt. Express **13**(17), 6550–6557 (2005).

16. B. Weichelt, A. Voss, M. Abdou Ahmed, and T. Graf, "Enhanced performance of thin-disk lasers by pumping into the zero-phonon line," Opt. Lett. **37**(15), 3045–3047 (2012).

17. C. Momma, S. Nolte, G. Kamlage, F. von Alvensleben, and A. Tünnermann, "Beam delivery of femtosecond laser radiation by diffractive optical elements," Appl. Phys., A Mater. Sci. Process. **67**(5), 517–520 (1998).

18. T. Metzger, A. Schwarz, C. Y. Teisset, D. Sutter, A. Killi, R. Kienberger, and F. Krausz, "High-repetition-rate picosecond pump laser based on a Yb:YAG disk amplifier for optical parametric amplification," Opt. Lett. **34**(14), 2123–2125 (2009).

19. J. Dörring, A. Killi, U. Morgner, A. Lang, M. Lederer, and D. Kopf, "Period doubling and deterministic chaos in continuously pumped regenerative amplifiers," Opt. Express **12**(8), 1759–1768 (2004).

20. R. W. Boyd, *Nonlinear optics*, 3rd ed. (Academic Press, 2008).

21. L. Sudrie, A. Couairon, M. Franco, B. Lamouroux, B. Prade, S. Tzortzakis, and A. Mysyrowicz, "Femtosecond laser-induced damage and filamentary propagation in fused silica," Phys. Rev. Lett. **89**(18), 186601 (2002).

22. A. Couairon, M. Franco, G. Méchain, T. Olivier, B. Prade, and A. Mysyrowicz, "Femtosecond filamentation in air at low pressures. Part I: Theory and numerical simulations," Opt. Commun. **259**(1), 265–273 (2006).

23. S. Prinz, M. Häfner, M. Schultze, C. Y. Teisset, R. Bessing, K. Michel, R. Kienberger, and T. Metzger, "Active pump-seed-pulse synchronization for OPCPA with sub-2-fs residual timing jitter," Opt. Express **22**(25), 31050–31056 (2014).

24. J. Moses, C. Manzoni, S.-W. Huang, G. Cerullo, and F. X. Kärtner, "Temporal optimization of ultrabroadband high-energy OPCPA," Opt. Express **17**(7), 5540–5555 (2009).

25. T. Stanislauskas, I. Balčiūnas, V. Tamuliene, R. Budriūnas, and A. Varanavičius, "Analysis of parametric fluorescence amplified in a noncollinear optical parametric amplifier pumped by the second harmonic of a femtosecond Yb. KGW laser," Lith. J. Phys. **56**(1), 1 (2016).

26. J. Ahrens, O. Prochnow, T. Binhammer, T. Lang, B. Schulz, M. Frede, and U. Morgner, "Multipass OPCPA system at 100 kHz pumped by a CPA-free solid-state amplifier," Opt. Express **24**(8), 8074–8080 (2016).

27. A. Giree, M. Mero, G. Arisholm, M. J. Vrakking, and F. J. Furch, "Numerical study of spatiotemporal distortions in noncollinear optical parametric chirped-pulse amplifiers," Opt. Express **25**(4), 3104–3121 (2017).

28. A. Renault, D. Z. Kandula, S. Witte, A. L. Wolf, R. T. Zinkstok, W. Hogervorst, and K. S. E. Eikema, "Phase stability of terawatt-class ultrabroadband parametric amplification," Opt. Lett. **32**(16), 2363–2365 (2007).

29. S. Hädrich, J. Rothhardt, M. Krebs, S. Demmler, J. Limpert, and A. Tünnermann, "Improving carrier-envelope phase stability in optical parametric chirped-pulse amplifiers by control of timing jitter," Opt. Lett. **37**(23), 4910–4912 (2012).

30. A. Baltuska, M. Uiberacker, E. Goulielmakis, R. Kienberger, V. S. Yakovlev, T. Udem, T. W. Hansch, and F. Krausz, "Phase-controlled amplification of few-cycle laser pulses," IEEE J. Sel. Top. Quantum Electron. **9**(4), 972–989 (2003).

31. F. Tavella, K. Schmid, N. Ishii, A. Marcinkevičius, L. Veisz, and F. Krausz, "High-dynamic range pulse-contrast measurements of a broadband optical parametric chirped-pulse amplifier," Appl. Phys. B **81**(6), 753–756 (2005).

32. B. Bernhardt, A. Ozawa, A. Vernaleken, I. Pupeza, J. Kaster, Y. Kobayashi, R. Holzwarth, E. Fill, F. Krausz, T. W. Hänsch, and T. Udem, "Vacuum ultraviolet frequency combs generated by a femtosecond enhancement cavity in the visible," Opt. Lett. **37**(4), 503–505 (2012).

33. M. Lewenstein, P. Balcou, M. Y. Ivanov, A. L'Huillier, and P. B. Corkum, "Theory of high-harmonic generation by low-frequency laser fields," Phys. Rev. A **49**(3), 2117–2132 (1994).

34. S. Demmler, J. Rothhardt, S. Hädrich, M. Krebs, A. Hage, J. Limpert, and A. Tünnermann, "Generation of high-photon flux-coherent soft x-ray radiation with few-cycle pulses," Opt. Lett. **38**(23), 5051–5054 (2013).

35. A. Baltuska, T. Udem, M. Uiberacker, M. Hentschel, E. Goulielmakis, Ch. Gohle, R. Holzwarth, V. S. Yakovlev, A. Scrinzi, T. W. Hänsch, and F. Krausz, "Attosecond control of electronic processes by intense light fields," Nature **421**(6923), 611–615 (2003).

36. H. Fattahi, H. G. Barros, M. Gorjan, T. Nubbemeyer, B. Alsaif, C. Y. Teisset, M. Schultze, S. Prinz, M. Haefner, M. Ueffing, A. Alismail, L. Vámos, A. Schwarz, O. Pronin, J. Brons, X. T. Geng, G. Arisholm, M. Ciappina, V. S. Yakovlev, D.-E. Kim, A. M. Azzeer, N. Karpowicz, D. Sutter, Z. Major, T. Metzger, and F. Krausz, "Third-generation femtosecond technology," Optica **1**(1), 45 (2014).

37. C. Teisset, M. Schultze, R. Bessing, M. Haefner, S. Prinz, D. Sutter, and T. Metzger, "300 W Picosecond Thin-Disk Regenerative Amplifier at 10 kHz Repetition Rate," in *Advanced Solid State Lasers*, JTh5A.1.

38. M. Schultze, C. Wandt, S. Klingebiel, C. Y. Teisset, M. Häfner, R. Bessing, T. Herzig, S. Prinz, S. Stark, K. Michel, and T. Metzger, "Toward Kilowatt-Level Ultrafast Regenerative Thin-Disk Amplifiers," in *Advanced Solid State Lasers*, ATu4A.4.
39. T. Nubbemeyer, M. Kaumanns, M. Ueffing, M. Gorjan, A. Alismail, H. Fattahi, J. Brons, O. Pronin, H. G. Barros, Z. Major, T. Metzger, D. Sutter, and F. Krausz, "1 kW, 200 mJ picosecond thin-disk laser system," Opt. Lett. **42**(7), 1381–1384 (2017).

1. Introduction

Short pulses in the few-cycle regime are nowadays routinely used in ultrafast science to generate isolated attosecond pulses in the extreme-ultraviolet (XUV) spectral region via high harmonic generation (HHG), enabling time resolved measurements in matter on the atomic scale [1–3].

Most of the experiments are still performed using Titanium-sapphire based amplifiers with mJ-level pulse energies at kHz repetition rates. In such systems, pulse durations remain confined to around 20 fs due to gain narrowing. Thus, additional spectral broadening in hollow core fibers is required to approach the few-cycle limit, which ultimately restrains the achievable pulse energy to a few mJ [4–6]. To further push the frontiers in attosecond science, new powerful, stable and compact laser sources are needed.

Higher pulse energies paired with multi-kHz repetition rates are desirable to generate a high XUV photon flux and increase the signal to noise ratio [7], potentially enabling XUV-XUV pump-probe experiments [8]. Once the laser pulse duration narrows to a few optical cycles, a stable carrier-envelope phase (CEP) becomes crucial in most experiments [9].

A promising technology which potentially meets those requirements is optical parametric chirped pulse amplification (OPCPA). OPCPA enables direct amplification of large bandwidths with high gain, simultaneously preserving the CEP of the seed pulses [10]. The instantaneous nature of the process reduces thermal effects inside the nonlinear medium and allows for high power pumping with no amplified emission outside the temporal window of the pump pulse.

OPCPA output powers as high as 22 W at 1 MHz repetition rate (22 µJ of pulse energy) [11] and 15 W at 300 kHz (50 µJ) were demonstrated so far [12]. At repetition rates as low as 10 Hz, the generation of pulse energies up to 130 mJ is feasible in large laser facilities [13]. Recently, record values of 53 W at 1 kHz (53 mJ) were achieved by combining multiple high energy pump sources and a total of 6 OPCPA stages [14].

In this publication we present a compact high-power few-cycle OPCPA system with excellent long-term stability. Pulse energies of >1.8 mJ are combined with high repetition rates of 6 kHz, leading to an average output power of more than 10 W. CEP-stable pulses with an average pulse duration as short as 7.2 fs are generated, corresponding to peak powers of more than 160 GW. The system is seeded by a commercial Titanium-sapphire oscillator and pumped by an optically synchronized Yb-based thin-disk regenerative amplifier. The overall conversion efficiency is limited by nonlinear effects in air at high pump peak powers, which is confirmed by our numerical simulations and proven experimentally. In a first experiment, the system is used to generate high harmonics in a Neon gas jet.

2. System setup and experimental results

The schematic outline of the complete system is shown in Fig. 1. Every subsystem with their related experimental results is described in detail in this section.
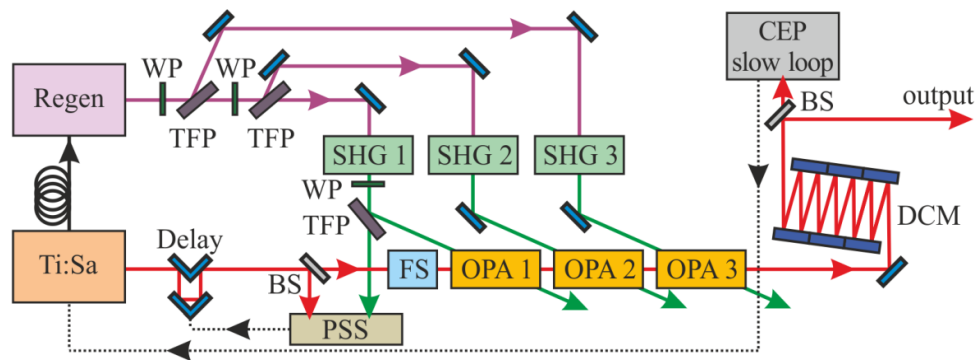
Fig. 1. Schematic layout of the OPCPA system. Ti:Sa: Titanium-sapphire oscillator, Regen: regenerative amplifier, BS: beam splitter, WP: waveplate, TFP: thin-film polarizer, SHG: second harmonic generation, PSS: pump-seed synchronization, FS: fused silica stretcher, OPA: optical parametric amplifier, CEP slow loop: carrier-envelope phase slow-loop stabilization, DCM: double-chirped mirror compressor.

2.1 Seed source

A commercial Titanium-sapphire oscillator (venteon dual CEP) serves as the master seed source, simultaneously seeding the parametric amplification chain and the regenerative amplifier. An all-optical synchronization is hence achieved between the interacting pulses [15].

The oscillator delivers up to 200 mW output power at a repetition rate of 80 MHz. Measured at −10 dB, the spectral bandwidth spans over 380 nm at a central wavelength of 800 nm. The associated Fourier-limited pulse duration is below 5 fs.

An f-to-2f interferometer, set up after the oscillator, detects the CEP from the direct beat occurring between the extreme wings of the octave-spanning spectrum. Stabilization is realized by an active feedback to the pump laser with a residual phase noise below 70 mrad.

The 1030 nm-seed for the regenerative amplifier is derived directly from the oscillator spectrum and sent to a 3-stage fiber amplification chain (Fig. 2) with integrated pulse picker. At the output, the pulse energy reaches 25 nJ at 1 MHz repetition rate. Additionally, the pulses are stretched in time by a fiber Bragg grating (FBG) introducing a dispersion of 384 ps/nm.

2.2 Thin-disk regenerative amplifier

The regenerative amplifier is based on an industrial thin-disk laser head by TRUMPF Laser. The active medium is a ~1/10 mm thin Ytterbium-doped disk mounted on a diamond heat sink for efficient cooling. The disk is continuously pumped with up to 400 W by laser diodes stabilized at a wavelength of 969 nm using volume Bragg gratings. This permits the direct pumping into the zero-phonon line, significantly reducing the heat load compared to the conventional 940 nm-pumping. With reduced diffraction losses from thermally-induced phase distortions, higher laser efficiency can therefore be attained [16]. The pump light is fiber-coupled to the thin-disk unit and imaged onto the disk 18 times via a parabolic retro-reflector to guarantee efficient absorption.
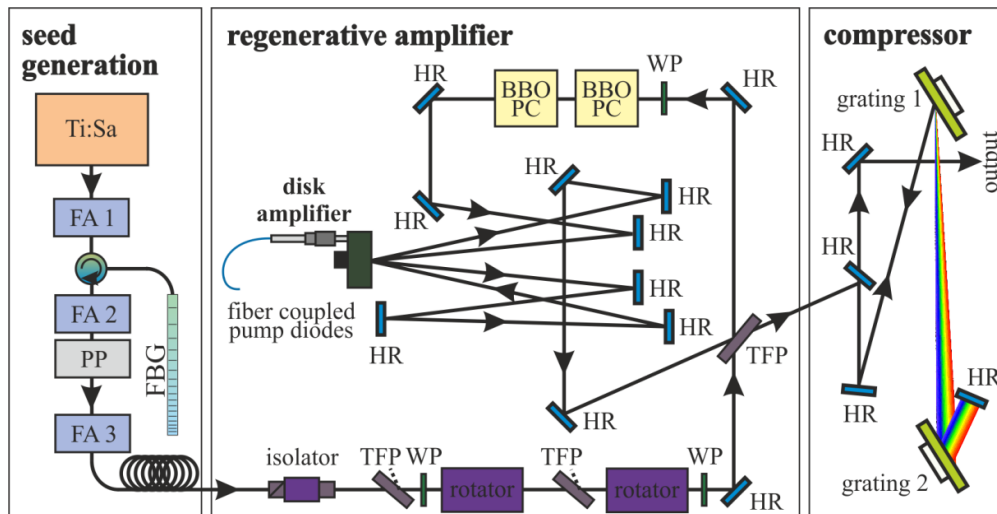
Fig. 2. Schematic setup of the regenerative amplifier. Ti:Sa: Titanium-sapphire oscillator; FA: fiber amplifier; FBG: fiber Bragg grating; PP: pulse picker; TFP: thin film polarizer; WP: wave plate; HR: highly reflective mirror; BBO PC: β-barium borate Pockels cell.

Figure 2 illustrates the schematic setup of the regenerative amplifier. The fiber-coupled front end is protected against back-reflections from the amplifier by three optical isolation stages. The cavity is set up as a ring with the disk arranged as a folding mirror. Two Pockels cells, each containing a z-cut β-barium borate (BBO) crystal, switch the pulses in and out of the cavity. The crystal is 20 mm long with an aperture of 12 mm, which corresponds to a quarter-wave voltage of 16 kV. The pulse passes the disk twice per roundtrip with an overall of 130 roundtrips, operating close to energy saturation. With a calculated B-Integral [17] of 1.1, no significant nonlinearities arise during the amplification process. After amplification, recompression is performed with two dielectric gratings (1760 lines/mm) separated by a normal distance of 900 mm in a double-pass near-Littrow configuration with an optical efficiency > 94%. The dispersion coefficients of the compressor are matched to those of the FBG up to the 4th order to minimize the residual phase and ensure a clean temporal pulse profile.

The output characteristics after compression are shown in Fig. 3(a). The total compressed output power reaches more than 170 W with a slope efficiency of 57%. Since the amplifiers repetition rate is set close to the inverse upper state lifetime of the gain medium, bifurcation of the output pulses occurs [18,19]. In the measured bifurcation diagram in Fig. 3(b), the onset of chaotic amplification emerges at a pump power $P_{pump} > 150$ W while stable period-doubling occurs above 350 W. In this regime, every second pulse is suppressed to < 1.5% of the main pulse, resulting in an effective repetition rate of 6 kHz and a main pulse energy of 28.3 mJ with pulse-to-pulse energy fluctuations below 0.7% RMS, recorded over several hours. The second-order autocorrelation reveals a clean Gaussian profile, exhibiting only minor side wings which originate from uncompensated higher-order dispersion (Fig. 3(c)). Accordingly, the pulse duration is evaluated to be 1.36 ps. The excellent beam quality is attested by M^2 values of 1.22 in the horizontal and 1.41 in the vertical plane, measured according to ISO 11146. Figure 3(d) presents the measurement together with the far-field beam profile.
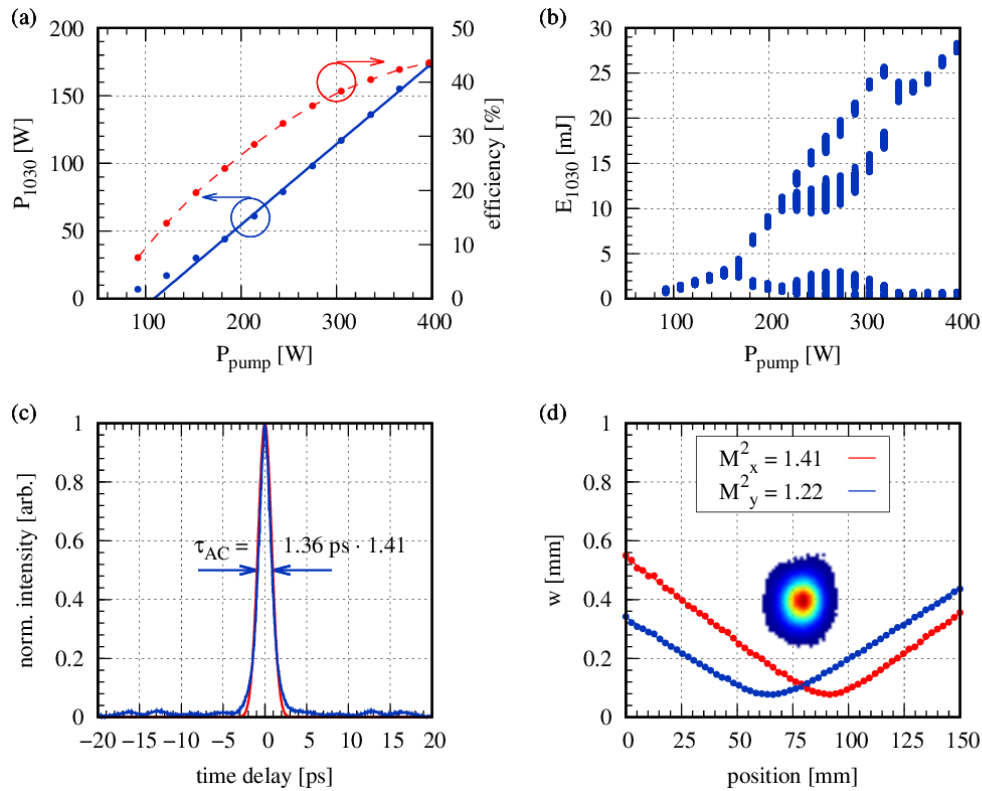
Fig. 3. Measurements on the regenerative amplifier: (a) compressed output power (solid line) and efficiency (dashed line) at different pump powers, (b) bifurcation diagram, (c) autocorrelation trace (blue) and Gaussian fit (red), (d) measured caustic and M^2 in horizontal and vertical plane with far field beam profile.

2.3 Second harmonic generation

Because nonlinear effects in air are becoming a primary concern at those peak powers, the infrared beam is split up right after the regenerative amplifier into three arms using a set of half-wave plates and thin-film polarizers. In addition the three frequency-doubling stages are placed as close as possible to the OPA. Each second harmonic generation (SHG) stage consists of a 2 mm-short Lithium triborate (LBO) crystal, stabilized to 40 °C by a temperature-controlled copper mount to ensure long-term phase matching. The intensity of the fundamental pulse is chosen to saturate the conversion process, resulting in low pulse-to-pulse energy fluctuations $E_{515,RMS}$. In Table 1, the major parameters for every SHG-stage are listed.

Table 1. Parameters used for second harmonic generation in the three SHG stages. In every stage, a 2 mm-short LBO crystal is employed.

	E_{1030} [mJ]	E_{515} [mJ]	Eff [%]	I (GW/cm^2)	$E_{515,RMS}$ [%]	B_{1030}
SHG 1	0.110	0.066	60.0	~100	0.74	0.50
SHG 2	10.54	5.04	47.8	~80	0.89	0.93
SHG 3	15.72	8.20	52.2	~80	0.98	0.72
Total	26.37	13.306	50.5	-	-	-

2.3.1 Conversion efficiency limitations

From Table 1, a significant change in conversion efficiency can be observed among the successive SHG stages. The decrease is attributed to the optical Kerr effect in air, leading to self-focusing and nonlinear phase distortions of the fundamental beam during propagation. To compare the influence of the nonlinearities, the accumulated nonlinear phase, i.e. the B-Integral, is calculated for each SHG stage.

The calculation is initiated at the output of the last compressor grating, where the pulse duration is the shortest. The beam path to the first TFP in the OPCPA setup is around 3 m. From there on, the propagation distances to SHG 1, SHG 2 and SHG 3 are 2 m, 4 m and 5 m respectively. The effects of the TFPs were included, when necessary.

It is found that the B-integral is below 1 in every beam path and thus lower than in the regenerative amplifier. However, the beams are subject to the Kerr effect due to the high peak powers P_{peak}. In the second and third arm, P_{peak} exceeds the critical peak power in air at 1030 nm, $P_{crit} \approx 4$ GW [20], by a factor of 2 and 3 respectively. The effect comes to light in Fig. 4, where the beam propagation in SHG 3 is simulated. Those plots present the evolution of the spatial beam profile over 5 m propagation in air for the two cases of (a) an initially collimated and (b) a divergent beam ($\theta = 0.5$ mrad). This calculation considers a 15 mJ-pulse at $\lambda = 1030$ nm with $P_{peak} > 3 \cdot P_{crit}$. The simulation numerically integrates the evolution of the electric field envelope in the presence of linear (dispersion and diffraction) and nonlinear (self-phase modulation, Raman scattering, multi-photon ionization and plasma formation) terms [21]. The material parameters for air are taken from [22]. The dashed line in the 2D plot represents the evolution of the $1/e^2$-beam width and the solid line that of the full width at half maximum (FWHM) beam width. The bottom graph shows the relative energy content E_{rel} in the FWHM area.
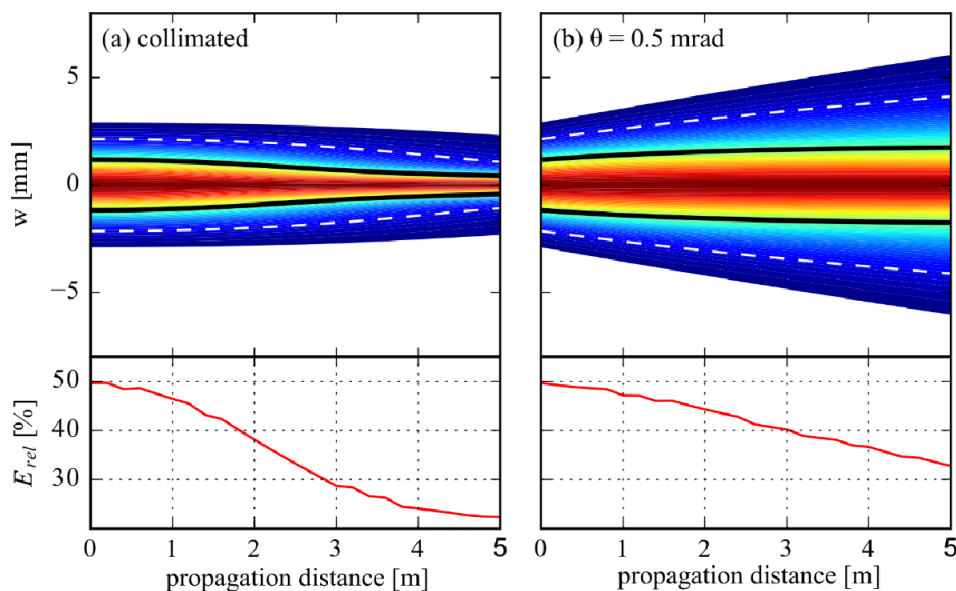

Fig. 4. Simulated pulse propagation in air with $E_{1030} = 15$ mJ for a collimated (a) and a divergent beam with $\theta = 0.5$ mrad (b). The upper graph shows the spatial beam evolution with the $1/e^2$-beam width marked as dashed and the FWHM as a solid line. The bottom graph reveals the relative energy content E_{rel} in the FWHM area. An increasing energy drain from the beam center towards the diverging outer area decreases the SHG conversion efficiency.

The self-focusing effect is clearly visible in the collimated case (a), where the beam starts to collapse after ~1 m of propagation.

As the beam size shrinks, the beam intensity increases, eventually leading to optical damages. At the same time, the relative amount of energy contained in the FWHM, E_{rel}, decreases. This effect can be partially counteracted in case of a divergent beam (b), where the energy drain counteracts the Kerr lens. As a result, the diverging beam has a quasi-collimated central part of constant FWHM. This approach allows operating the subsequent nonlinear stages safely, but to the detriment of the conversion efficiency. The SHG conversion efficiency is limited due to energy loss from the intense central part and due to nonlinear phase front distortions, as it can be seen in Fig. 5(a) in the spectral domain. Compared to the flat-phased Gaussian input, the spectrum is slightly broadened with a significantly altered phase, preventing perfect phase matching inside the SHG crystal.

The influence of the nonlinear propagation on the SHG efficiency is tested with help of SHG 3. Instead of splitting the pump pulse after the compressor, the output energy from the regenerative amplifier is limited directly to 15.7 mJ, which is sent completely into SHG 3. Reducing the pulse energy reduces the B-integral to $B_{1030} = 0.58$. The measured conversion curve is shown in Fig. 5(b) and is compared to the high-power case. Reducing the pump energy increases the efficiency by more than 5%. As both B-integral values are fairly small, the reduced efficiencies are attributed mainly to the energy loss from the beam center.

To attain high conversion efficiencies, it is therefore imperative to minimize the nonlinearities along the beam. In our setup, this is achieved by splitting up the fundamental pulse as close as possible to the OPCPA input (reducing the peak power in every arm), placing the SHG stages close to the OPCPA stages (because P_{crit} scales with λ^2) and using detuned telescopes to prevent a catastrophic beam collapse.
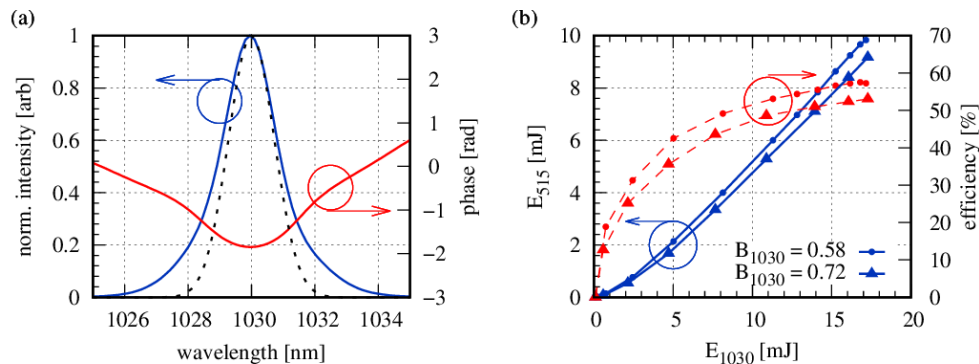

Fig. 5. (a) Input spectrum (dashed) and simulated (solid) spectral intensity distribution and phase for the beam propagation according to Fig. 4(b). The B-integral after 5 m is $B_{1030} = 0.34$. (b) Measured characteristics of SHG 3 under the influence of strong and weak nonlinear effects, characterized by the B-integral B_{1030}. The predominant reason for the reduced efficiency is the energy drain from the quasi-collimated beam center.

2.4 Pump seed synchronization (PSS)

Precise temporal overlap between the pump and seed pulses is an essential parameter in any OPA and a prerequisite for stable long-term operation. Despite the intrinsic optical synchronization between pump and seed source, timing fluctuations arise from thermal drifts, air fluctuations or vibrations. The amplification inside the regenerative amplifier is associated with a several-hundred-meter-long beam path, making it an acute source of instabilities.

To lock the overlap of pump and seed pulses in time, an active synchronization system based on a spectrally resolved OPA has been developed [23]. A minor fraction of the beams is allocated to this purpose: 6 µJ from the pump is split off after SHG 1, while a seed energy as low as 400 pJ is used. With this technique, the remaining timing jitter is reduced below 10 fs RMS which is less than 1% of the pump-pulse duration. This precise synchronization guarantees stable amplification conditions from pulse to pulse.

2.5 Optical parametric chirped pulse amplification

Scaling of the seed pulses to the multi-mJ level takes place in three consecutive OPA stages. BBO crystals cut at θ = 24° are implemented in each stage inside a temperature-stabilized copper holder. A noncolinear internal angle of ~2.44° between the interacting beams is chosen to obtain broadband phase-matching. Prior to the first stage, 20% of the seed energy is reserved for the PSS. The remaining 80% are stretched in a 20 mm-short fused silica substrate to about half the pump-pulse duration. Fine compensation of the residual dispersion is carried out by a pair of CaF-wedges with an insertion thickness of ~2 mm. Thanks to the material dispersion of the nonlinear crystals, no additional adjustment of the seed pulse duration is necessary between the OPA stages in this concept. Because the temporal region of significant gain in relation to the pump pulse increases with a smaller peak gain [24], the seed duration is inherently adjusted throughout the amplifier chain to match the gain region in every stage, efficiently extracting the pump energy without a loss in bandwidth. The experimental results at every OPA stage are summarized in Table 2. These values will be commented in detail hereafter.

Table 2. Experimental parameters in the three OPA stages.

	E_{seed} [mJ]	E_{pump} [mJ]	E_{signal} [mJ]	I_{pump} [GW/cm^2]	Gain	Eff [%]	L [mm]	Geom.
OPA 1	5.2E-7	0.06	5.7E-3	~120.0	1E4	9.6	3.0	PVWC
OPA 2	4.6E-3	5.04	0.78	~45.0	169	15.4	2.0	PVWC
OPA 3	0.55	8.20	2.02	~65.0	3.7	18.0	3.0	TPM

Losses from optics in the beam path reduce the seed energy in the first OPA stage to 520 pJ. The first amplification takes place in a 3 mm-short BBO crystal oriented in a Poynting-vector-walk-off-compensation (PVWC) geometry. Using 60 µJ (360 mW) from SHG 1 a pump intensity of ~120 GW/cm^2 is reached, enabling broadband amplification down to a Fourier-limited pulse duration of 6.2 fs. The seed pulses are amplified to 5.7 µJ (34.2 mW), corresponding to a gain of > 10^4 and an optical efficiency of 9.6%.

The complete output of SHG 2 (5.04 mJ / 30.2 W) is sent to the second stage (OPA 2). Here, a 2 mm-short BBO crystal with an aperture of 15 mm is implemented again in PVWC. The pump intensity is significantly reduced compared to the previous stage because of the higher seed level. An intermediate pulse energy of 780 µJ (4.68 W) is achieved with an optical efficiency of 15.4%.

The third amplification stage (OPA 3) finally boosts the energy to 2.02 mJ (12.12 W), with 8.2 mJ of pump energy converted in SHG 3. The 3 mm-short BBO is pumped at an intensity of ~65 GW/cm^2 and the conversion efficiency rises to 18.0%. In this stage, tangential-phase-matching (TPM) geometry proved to be favorable for a cleaner pulse recompression, inducing less higher-order phase. The efficiency in the two high-power OPA stages is again limited by nonlinear effects on the pump beams as described in section 2.3.1, which are even more pronounced at λ = 515 nm due to the quadratic wavelength-dependency of the critical peak power.

Finally, the pulses are compressed to 7 fs by 14 bounces on double-chirped mirror pairs, designed to match the dispersion of BBO and fused silica. This equals 2.5 optical cycles at the central wavelength of 810.7 nm. No additional active phase-shaping device is necessary in the setup to achieve a well compressed pulse. After compression, a final beamsplitter reflects 99% of the pulse energy to the output, resulting in a total compression efficiency of ~90%. The transmitted 1% is used in a common-path f-to-2f interferometer (Menlo Systems APS800) for slow-loop CEP-stabilization. Using white light generation in a thin sapphire plate, an octave-spanning spectrum is generated. The resulting spectral interference pattern is detected by a fast spectrometer. Despite the compression and outcoupling losses, the final output energy is as high as 1.8 mJ with an average power of 10.8 W.

To estimate the amount of parametric superfluorescence (PSF), the seed is first blocked in front of every OPA stage while pumping it at full power. In all three stages, the generated PSF power is below the noise level of the utilized powermeter. Second, the seed is blocked in front of the first stage and all OPAs are operated at their usual setpoint. Now the infinitesimal amount of PSF generated in OPA 1 serves as seed for the following stages and is further amplified up to 8.8 W, corresponding to ~81% of the total output power. However, the amount of PSF is significantly decreased in the seeded case. Taking into account the pulse compression of ~$2 \cdot 10^2$ and a typical gain quenching factor of 6 [25], the final pulse contrast between main pulse and PSF pedestal is estimated to be ~$6.6 \cdot 10^4$. This value is comparable to other high gain OPCPA systems [26, 11].

3. OPCPA output characteristics

3.1 Spectral and temporal properties

Figure 6 summarizes the output pulse characteristics of the 1.8 mJ output, measured with spectral phase interferometry (venteon SPIDER). As reference, the normalized seed spectrum is indicated in (a) with a 40 dB offset.
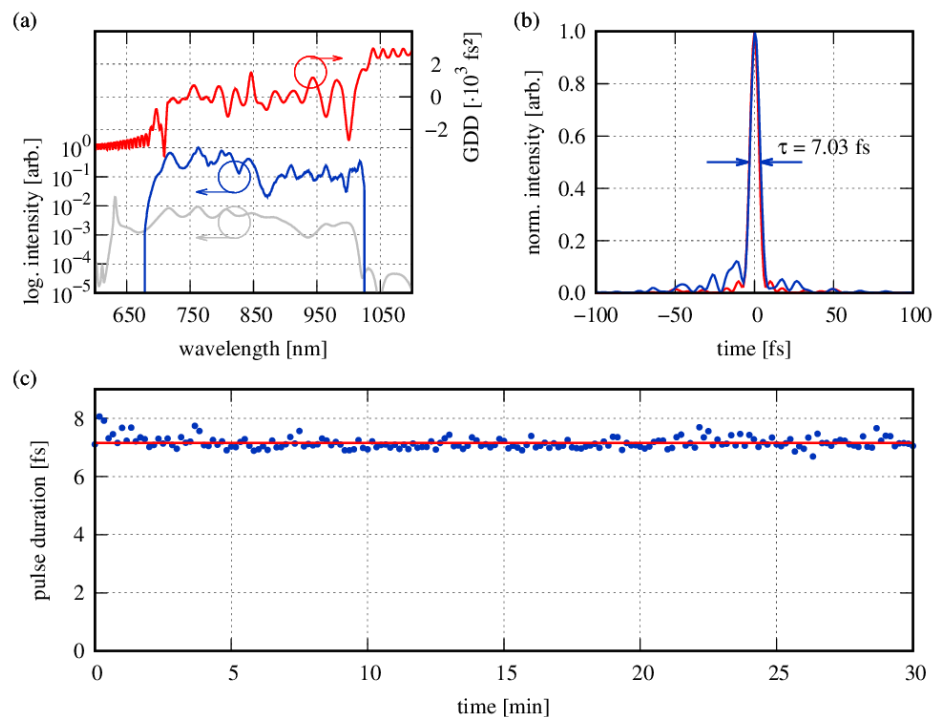

Fig. 6. OPCPA pulse characteristics, measured with SPIDER. (a) Seed spectrum (grey), fundamental spectrum (blue) and reconstructed GDD (red), (b) typical example of the reconstructed temporal pulse shape (blue) compared to the Fourier-limited pulse (red), (c) long-term pulse duration measurement with a mean pulse duration of 7.16 fs (red) and a standard deviation of only 199 as.

With a −10 dB-bandwidth of more than 300 nm around the central wavelength of 810.7 nm, a Fourier-limited pulse duration of 6.6 fs is supported, as shown in (a). The intensity dip at λ = 870 nm originates from parasitic second harmonic generation in OPA 1 and OPA 2, as expected from a PVWC geometry. No spectral broadening beyond the seed bandwidth is observed. Figure 6(b) presents a typical example of the reconstructed temporal pulse shape in blue. Some minor satellites are visible apart from the main pulse, due to uncompressed higher-order dispersion. Characterization of the pulses with a Wizzler

(Fastlite) confirmed the close to transform-limited pulse duration. The energy within the main pulse reaches more than 70%, resulting in a peak power of > 160 GW. The excellent long-term stability of the amplifier chain is attested in Fig. 6(c). Continuous pulse duration measurement every 10 s over a period of 30 minutes reveals a standard deviation of only 199 as at a mean pulse duration of 7.16 fs.

3.2 Pulse energy stability and caustic

The third OPA stage is operated in a heavily saturated regime, leading to an enhanced bandwidth and pulse-energy fluctuations as low as 1.8%, computed over 100000 consecutive pulses using a GHz-oscillopscope and a fast photodiode. Those benefits take a toll on beam quality dictated by the back-and-forth conversions between signal and pump. Since most high field experiments are performed in the focal plane, the focusability of the beam is investigated by measuring the focal beam profile and the caustic at different central wavelengths with the help of bandpass filters (FWHM 10 nm).

Two cases are investigated: (a) system operation without pumping the third OPA stage and (b) operation at full power. Figure 7(a) presents the near and far field beam profiles and the beam caustic in the first case, amplifying only in the first and second OPA stage. To analyze chromatic errors, the beam caustic is recorded at 750 nm, 850 nm and 950 nm in the vertical and horizontal plane. The second OPA is operated in a slightly saturated regime at the onset of back conversion, indicated by the central dip in the near field beam profile. In this configuration, a slightly higher pulse energy fluctuation of 2.2% has been measured at the output of the system. In the horizontal axis (top), all wavelengths are focused at the same plane, while in the vertical axis (bottom), a wavelength-dependent focal shift of $z_0(750 \text{ nm}) - z_0(950 \text{ nm}) = 0.33 \cdot z_r$ is observed, where z_r is the Rayleigh length at 850 nm and $z_0(\lambda)$ the position of the focal plane at the central wavelength λ. The measured M^2 values are close to those of the pump laser (compare Fig. 3(d)) and in the far field, a Gaussian beam profile is obtained. The circle marks the area around the beam center in which 80% of the total energy is contained. The small radius indicates a high energy confinement with low diffraction losses, attesting a good focusability.

Figure 7(b) shows the same measurement at full output power, pumping all OPA-stages. Despite a rather modulated near-field beam profile, a good beam quality is acquired in the far field, indicated by the spatial confinement of the energy. The wavelength-dependent focal shift in the vertical plane remains unchanged, whereas in the horizontal axis a focal shift of the same order ($0.33 \cdot z_r$) is measured. An increase of the M^2 values is observed which can be compensated by using shorter focal lengths to match the desired far-field spot size.

The characterization of the beam proves that even with a non-uniform beam profile a good focusability can be attained. Since all wavelengths are focused within the Rayleigh length, no detrimental influence on intensity dependant applications as e.g. HHG is expected. With the presented system parameters, a typical HHG intensity of $\sim 10^{15}$ W/cm^2 can be reached at a $1/e^2$-beam radius of w $\sim$100 µm.
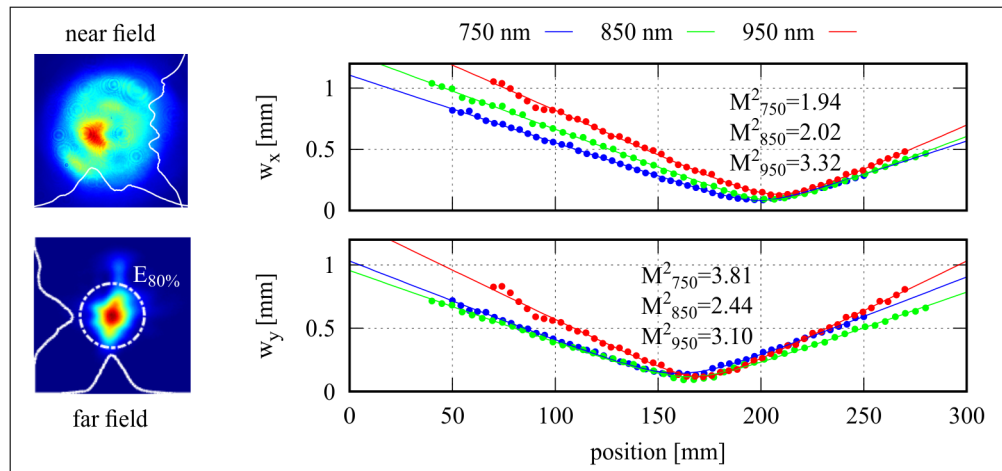
(a) OPA 3 unpumped
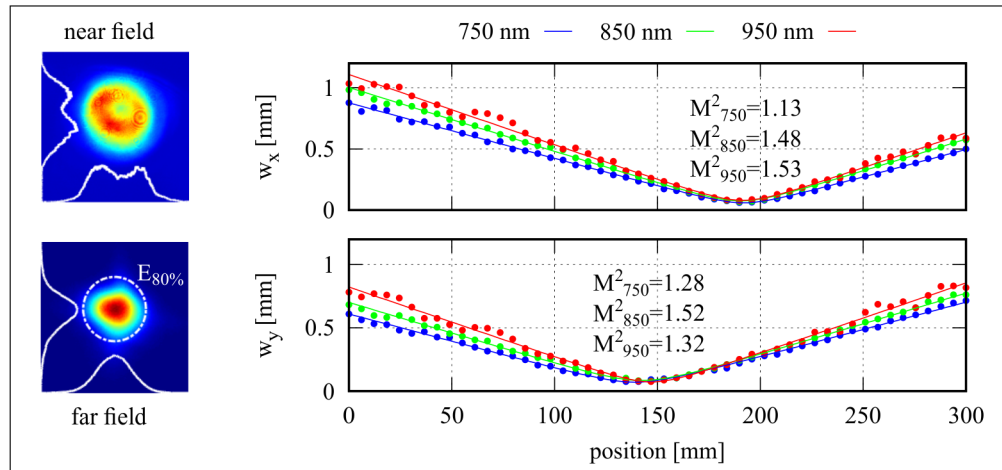
(b) all OPA stages

Fig. 7. Near and far field beam profile of the OPCPA and beam caustic in horizontal (top) and vertical axis (bottom) at different wavelengths. Bandpass filters (FWHM 10 nm) were used to select central wavelengths of 750 nm, 850 nm and 950 nm. The circle in the far field beam profile marks the area in which 80% of the total energy is confined. (a) OPA 3 left unpumped, (b) all OPA stages pumped.

3.3 Spatial chirp

Back-and-forth conversion between signal and pump in a saturated OPA as well as a pulse front-tilt between the involved beams are known to induce a spatial chirp on the beam profile [27]. As both effects are present in this system, the spatial chirp is investigated by scanning a 100 µm thin vertical slit through the near field beam, imaged to a spectrometer. The resulting spatially resolved spectral distribution is shown in Fig. 8. Every measured spectrum is normalized and plotted on a linear scale.
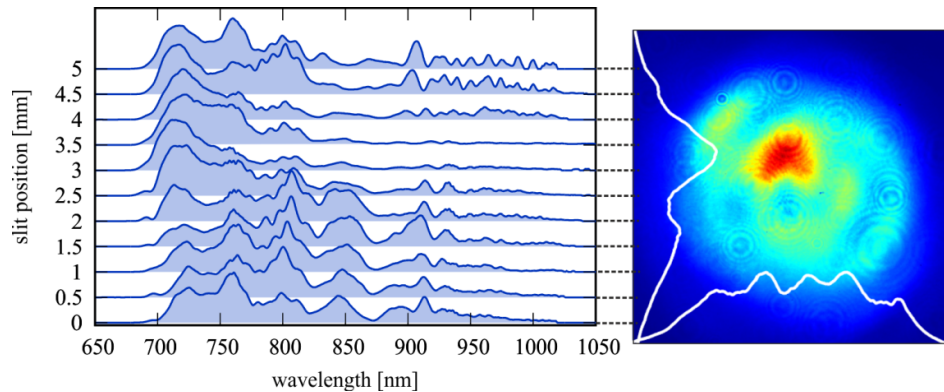
Fig. 8. Spatially resolved spectral distribution throughout the near field beam profile. A 100 μm thin slit imaged to a spectrometer was used to select different spatial slices of the beam. Every measured spectrum is normalized and plotted on a linear scale.

Apart from a dominant blue part in the area of highest intensity, only small variations are detected throughout the beam profile. It has already been shown in the previous sections that neither compressibility nor focusability of the beam is critically impaired by the measured spectral distribution. This confirms once more that the chosen oversaturated operating point represents a good compromise between enhanced stability and bandwidth gained at the cost of a small degradation of spatial beam homogeneity and M^2.

In general, a less modulated and spatially chirped beam profile could be potentially obtained by operating the OPA stages in a less saturated regime, avoiding back-and-forth conversion between signal and pump. However, a simultaneous decrease in spectral bandwidth and pulse energy stability is expected.

3.4 Carrier envelope phase stability

The stabilized CEP is detected after pulse compression by the integrated f-to-2f interferometer (Menlo Systems APS800), delivering a feedback signal to the Titanium-sapphire seed oscillator. An integration time of 167 μs is set for the spectrometer, hence integrating over a single pulse only. Figure 9 compares the results for the free running (shaded area) and stabilized case. The benefits of the stabilization are highlighted by the large fluctuations of the CEP when the slow-loop feedback is disabled. After switching on the stabilization, the residual phase noise was reduced below 169 mrad RMS over a 5-min-long record.
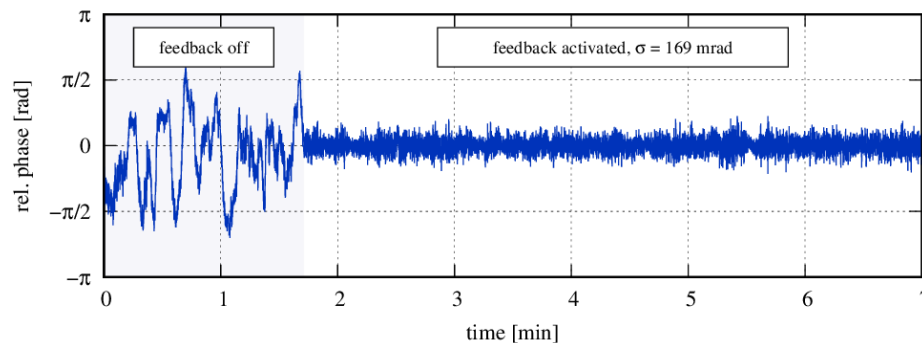

Fig. 9. CEP drift at the systems output in the free-running case (shaded area) and with activated feedback from the slow-loop.

Considering the excellent pump-energy stability of < 1% and the remaining timing jitter of < 10 fs, contributions of pump-intensity coupling [28] and pump-seed-timing instabilities [29] are negligible compared to the CEP-noise of the oscillator of 70 mrad. The majority of the detected CEP-fluctuations is thus attributed to detection noise in the employed f-to-2f interferometer from amplitude-to-phase coupling in the process of spectral broadening. A phase shift of 84 mrad was observed by Baltuška et al. to accompany a pulse-energy jump of only 1% [30]. Taking into account the systems long-term energy fluctuations of 1.8%, a detection limit > 150 mrad is expected which limits the final CEP noise.

3.5 Temporal pulse contrast

Using a home-build third harmonic generation autocorrelator, the pulse contrast on a timescale of 100 ps was examined (Fig. 10). A photodiode amplifier used at different amplification levels allows for a measurement contrast up to 10^7. Due to unmatched dispersion in both arms of the measurement device, the contrast between the main pulse and the PSF pedestal currently cannot be resolved. However, any pre- or post-pulses are clearly identified.

Owing to the ultrashort-pulsed pumping, the main pulse exhibits no temporal pedestal outside the ~1 ps-short pump window. A post pulse at $\tau = 21.2$ ps with a corrected intensity of $I/I_0 = 2.5 \cdot 10^{-4}$ is identified which likely originates from the backside reflection of the second OPA crystal. The less intense pulses at 0.9 ps, 1.8 ps and −28 ps constitute measurement artifacts introduced by the nonlinear crystals inside the autocorrelator.

The autocorrelation indicates an isolated main pulse of high contrast which contains almost the full energy. Long pedestals from PSF are absent but are common when using longer pump-pulse durations [31].
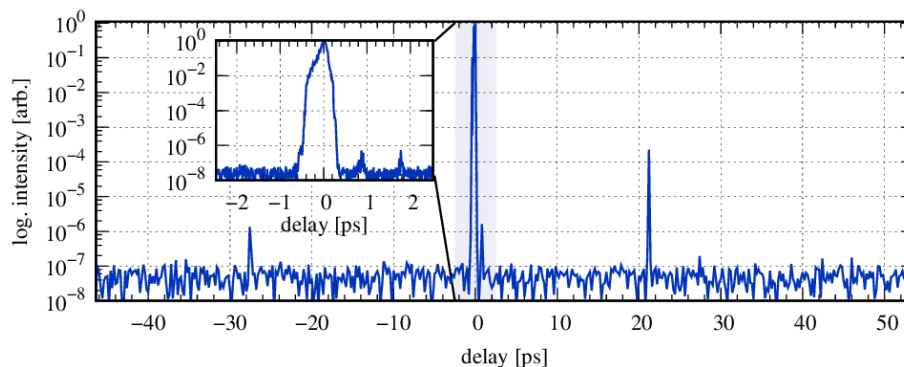

Fig. 10. Third harmonic autocorrelation of the OPCPA output. Pre-pulses are located at negative delays, post pulses at positive delays. A high resolution measurement (inset) around the main pulse attests of the excellent contrast.

3.6 Power stability

The output power of the OPCPA system was recorded over 8 hours of operation at 10.8 W, as plotted in Fig. 11. Only one minor spatial alignment of the pump beam was performed after 3.4 h. For the periods before and after the alignment, the RMS power fluctuation was measured to be 1.8% only, proving the excellent long-term stability of the system.
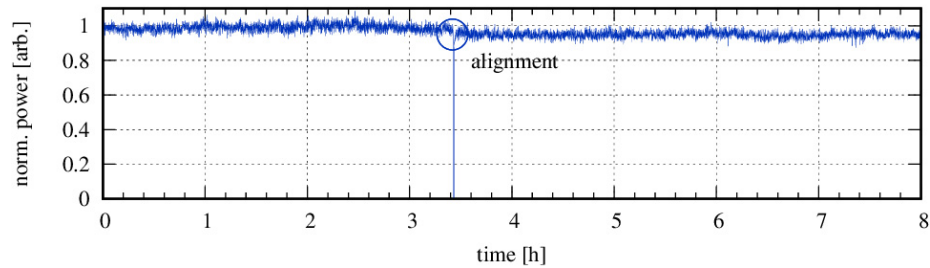
Fig. 11. Long-term power measurement of the OPCPA output power. At t = 3.4 h, spatial realignment of the pump beam was performed.

4. High harmonic generation

4.1 Experimental setup

In a proof-of-principle experiment, HHG in Neon (Ne) was demonstrated. The experimental setup consisted of three differentially pumped vacuum chambers, used for generation, spectral filtering and detection of the signal, respectively. To prevent damage to the vacuum entrance window [32], the final pulse compression was performed only inside the vacuum chamber by passing two double-chirped mirror pairs with a total of 4 bounces, while the number of bounces inside the OPCPA compressor was reduced accordingly. For dispersion fine tuning, a pair of fused silica wedges was mounted before the entrance window under Brewster's angle. A spherical mirror with f = 700 mm focused the collimated beam to a spotsize of ~100 μm. In the focal plane a ceramic nozzle with an aperture of 300 μm and a 1 mm internal diameter was mounted on an XYZ-stage., used to optimize the target position. About 100 mbar of Ne backing pressure resulted in ~10^{-3} mbar ambient pressure in the first chamber while in the detection chamber, 10^{-7} mbar could be maintained. In the early phase of the experiments, contamination by the use of metal targets resulted in transmission losses in the beamline and limited later on the available energy for HHG to only 0.87 mJ, resulting in ~500 TW/cm^2 on-target intensity.

After spectrally separating the high harmonics from the fundamental beam by inserting either a thin aluminum or zirconium filter foil, a home-built XUV-spectrometer was used to characterize the generated spectrum. Following an adjustable slit, a diffraction grating (Shimadzu 30-002, 1200 lines/mm) diffracted the beam onto a chevron-type microchannel plate (Beam Imaging Solutions, B0S-40-IAA-CH-MS), where the spectrum was converted with a phosphor screen (Beam Imaging Solutions, P-43) to the visible and imaged by a CCD-camera. A flip mirror, mounted in front of the XUV-spectrometer, was used to guide the signal to a second microchannel plate in combination with an imaging CCD-camera to monitor the beam profile.

4.2. Detection results

High harmonics up to the 61st order were generated in the described setup, corresponding to cut-off energies of 93 eV, shown in Fig. 12. The red line presents the detected spectrum, filtered by a 200 nm-thin aluminum foil, while the blue line presents the spectrum filtered by a 150 nm-thin zirconium foil. The target position was optimized to the maximum XUV flux on the microchannel plate after transmission through the zirconium foil, effectively selecting the short trajectory electrons for the HHG process [33]. As expected, according to the transmittance of each filter, different regions of the spectrum can be observed. Homogeneous beam profiles indicate phase matching of the process, so that comparable efficiencies to other state-of-the-art HHG sources on the order of ~10^{-9} are expected [34]. Higher cut-off energies can potentially be achieved in an optimized setup with increased energy transmission,

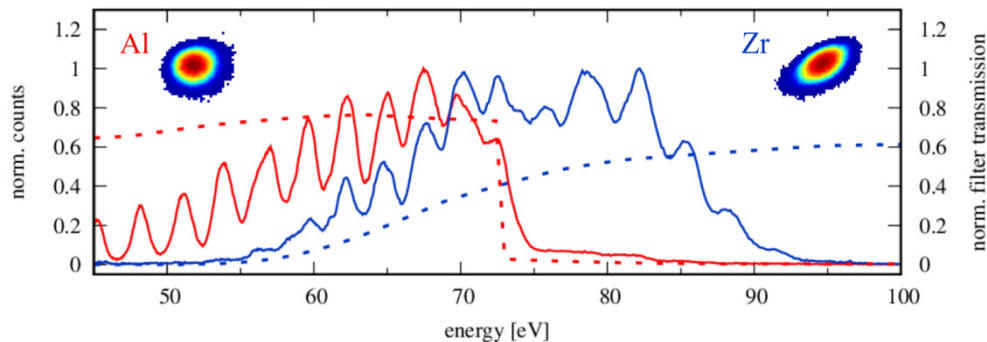optimized focal spot size and compensated beam astigmatism by means of cylindrical mirrors.

Fig. 12. HHG spectrum and spatial beam profile in Ne, measured after spectral filtering with aluminum (red) and zirconium (blue). The respective filter transmission curves are indicated as dotted lines. A cut-off energy of 93 eV is reached.

Several spectra were recorded with different CEP settings in the range from 0 to π, as shown in Fig. 13(a), filtered by a 150 nm-thin zirconium foil for isolating the harmonics above 60 eV. The CEP-dependence of the position of the harmonics, with a π period, is clear and in good agreement with the literature ([35], [9]) for few-cycle, CEP-stabilized pulses. The characteristic change of the spectral peak position in the cut-off region from even to odd harmonics, induced by a $\pi/2$ CEP-shift, is illustrated in Fig. 13(b). With CEP-stability and -control being proved, the system brings all requirements to be used in pump-probe experiments.
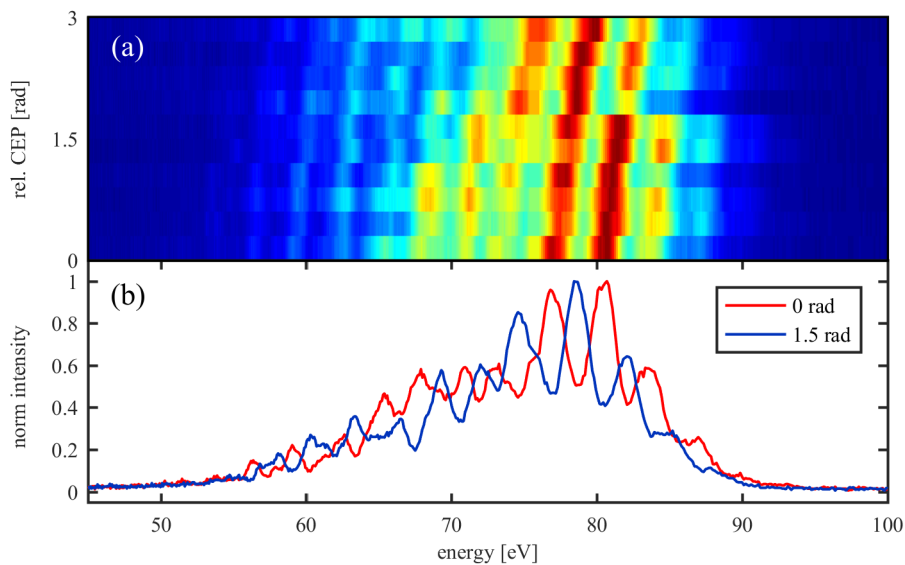

Fig. 13. Measured HHG spectrum as a function of the relative CEP of the driving pulses. (a) HHG spectra as a function of the relative CEP of the OPCPA pulses. The π-period of the spectral peaks is clearly visible. (b) Lineouts of two HHG spectra with a CEP change of ~$\pi/2$ between them.

5. Conclusion

We demonstrated an OPCPA system which combines high pulse energies of >1.8 mJ at 6 kHz repetition rate with a high average power of more than 10.8 W. CEP-stable few-cycle pulses with 7.2 fs pulse duration and a peak power beyond 160 GW are generated with excellent long-term power and energy stability. Those output characteristics render the system highly competitive to conventional Titanium-sapphire based amplifiers in the field of HHG, as proven by a first experiment yielding photon energies up to 93 eV generated in Neon with full CEP control.

Our experiments show that the supposed optimum pump pulse duration on the order of 1 ps [36] is not valid if the critical peak power in the propagation medium is exceeded, as nonlinear effects will notably diminish the overall efficiency. Further developments of our system will therefore address the minimization of nonlinearities present in the pump beam, e.g. by using a stretched pump pulse. This will simultaneously reduce the system complexity by decreasing the number of required SHG stages.

At this time, powerful pump lasers approaching the kW-level are maturing, delivering pulse energies of several hundreds of mJ with near-diffraction limited beam quality and extraordinary stability [37–39]. Implementing those next generation pump lasers in OPCPAs will be the upcoming step to break new ground in few-cycle laser sources and potentially explore unprecedented parameter regimes.